Ionization disequilibrium in K- and L-shell ions ⊞

D. T. Bishel ✉ iD ; E. V. Marley iD ; M. B. Schneider iD ; D. A. Liedahl iD ; R. F. Heeter iD ; M. E. Foord;
G. E. Kemp iD ; Y. Frank iD ; J. A. Emig; G. Pérez-Callejo iD ; P. M. Nilson iD ; D. A. Chin iD ; J. R. Rygg iD ;
G. W. Collins iD

Check for updates

View Online

Export Citation

CrossMark

Ionization disequilibrium in K- and L-shell ions ⓔⓟ

View Online　　　Export Citation　　　CrossMark

D. T. Bishel,[1,2,a)] ⓘ E. V. Marley,[3] ⓘ M. B. Schneider,[3] ⓘ D. A. Liedahl,[3] ⓘ R. F. Heeter,[3] ⓘ M. E. Foord,[3] ⓘ G. E. Kemp,[3] ⓘ
Y. Frank,[3] ⓘ J. A. Emig,[3] ⓘ G. Pérez-Callejo,[4] ⓘ P. M. Nilson,[2] ⓘ D. A. Chin,[1,2] ⓘ J. R. Rygg,[1,2,5] ⓘ and G. W. Collins[1,2,5] ⓘ

AFFILIATIONS

[1]Department of Physics and Astronomy, University of Rochester, Rochester, New York 14627, USA
[2]Laboratory for Laser Energetics, University of Rochester, Rochester, New York 14623, USA
[3]Lawrence Livermore National Laboratory, Livermore, California 94550, USA
[4]Departamento de Física Teórica, Atómica y Óptica, Universidad de Valladolid, Valladolid 47011, Spain
[5]Department of Mechanical Energy, University of Rochester, Rochester, New York 14627, USA

[a)]Author to whom correspondence should be addressed: dbishel@ur.rochester.edu

ABSTRACT

Time-gated Sc K-shell and Ge L-shell spectra are presented from a range of characterized thermodynamic states spanning ion densities of 10^{19}–10^{20}cm^{-3} and plasma temperatures around 2000 eV. For the higher densities studied and temperatures from 1000 to 3000 eV, the Sc and Ge x-ray emission spectra are consistent with steady-state calculations from the modern atomic kinetics model SCRAM. At the lower ion densities achieved through plasma expansion, however, the model calculations require a higher plasma temperature to reproduce the observed Ge spectrum. We attribute this to ionization disequilibrium of the Sc because the ionization time scales exceed the hydrodynamic timescale when the inferred temperatures diverge.

I. INTRODUCTION

Accurate models of atomic spectra enable the interpretation or design of systems where radiative energy transport is important, including astrophysical objects, high-Z ablation plasmas in laser-driven x-ray backlighters and inertial fusion hohlraums, and plasmas with highly transient excitation and ionization dynamics generated by intense x-ray free-electron laser pulses.[1] The accuracy of model calculations can only be verified by comparison to experimental spectra observed from a source with a characterized thermodynamic state.

The problem of model verification is particularly pronounced for non-local-thermodynamic-equilibrium (non-LTE) spectral models of multiple-electron ions. The complete set of atomic states increases exponentially with atomic number Z and exceeds current computational capabilities even for modest Z. Truncating schemes are, thus, employed to keep calculations tractable.[2] On the other hand, the included states must capture the dominant pathways of population flow, while maintaining sufficient detail of the quantum states to produce accurate spectral line energies and radiation transport. For the collisional-radiative rates themselves, either analytic approximations or empirical fits to data are used. Additional details have been previously reported.[2] Each of these approximations introduces uncertainty into the spectral model. Though great advances have been made in this field, recent international workshops have shown variation among different non-LTE codes when modeling spectra from open-shell configurations.[3,4]

Though non-LTE spectra have been studied at high-energy-density (HED) facilities for decades, the creation and characterization of a plasma suitable for model verification has proven to be difficult. Few datasets exist in the literature as a consequence. More recently, experiments using a sub-micrometer sample layer centrally buried in a low-Z tamper have been used at high-power laser facilities to create a homogeneous, expanding plasma at non-LTE conditions.[5–9] Both sides of the disk-like target are irradiated by high-power lasers to rapidly heat and expand the sample. The centrally buried layer is confined in the radial direction by the surrounding low-Z material, mitigating radial gradients and resulting in uniaxial expansion along the target normal. Axial gradients (along the expansion axis) in temperature are reduced once the plasma expands to subcritical densities since laser energy deposition is nearly uniform in the underdense plasma.[10,11] Axial tamping helps homogenize the density within the sample layer and slows the rate of expansion. Creation of spatially uniform conditions simplifies comparison between observed spectra and spectral model calculations because only a single thermodynamic state needs to be considered.

07 July 2023 14:53:19

However, there is a risk of ionization disequilibrium in the expanding plasma. When the thermodynamic timescale is faster than the ionization equilibration timescale, the ionization state will depart from its steady-state ("equilibrium") distribution and must be treated with a time-dependent calculation. This time-dependent ionization manifests in the measured spectrum. Using time-dependent spectra to validate steady-state calculations is improper and will give inaccurate results. Previous buried-layer studies have explored time-dependent ionization kinetics, but the conclusions have been varied. The threshold for steady-state ionization is a function of plasma temperature T_e, ion density n_i, nuclear charge, and ionization state through the ionization and thermodynamic time scales. Due to this multivariate dependence, it is not necessarily contradictory that previous publications have reached different conclusions of time-dependence for the particular target geometry and elements considered. Some studies have argued for the sufficiency of a steady state,[10] while others demonstrated the need for time-dependent ionization,[12] and still others indicated the presence of regions of steady-state and of time-dependent ionization within the same plasma.[13] Whether or not the ionization is time-dependent is idiosyncratic to the given platform. The potential for time-dependence must be considered when using the ionization state as a thermodynamic diagnostic. To the best of our knowledge, no observation of K-shell disequilibrium in axially tamped buried-layer targets has been published.

We present Sc K-shell and Ge L-shell spectra from a characterized buried-layer plasma. L-shell spectroscopy was recently proposed by Marley et al. as a thermodynamic diagnostic that is more sensitive to the plasma conditions than traditional K-shell measurements.[14] Additionally, the two species have different ionization equilibrium time scales due to their different nuclear charge and ionization state. To discriminate between the plasma temperature T_e and the observable ionization balance, we define T_Z to be the temperature required for a steady-state atomic kinetics calculation to reproduce the ionization balance evident in the observed spectrum. By fitting each spectrum with steady-state calculations from the atomic kinetics model SCRAM,[15] the T_Z of each species can be inferred. By construction, $T_Z = T_e$ for each species whose ionization is in thermal equilibrium with the circumfluent plasma. Spectra from the two species will test the spectral model more stringently than a single spectrum, while also providing a means to determine if the ionization distributions have attained a steady state.

The paper is organized as follows. In Sec. II, we describe the experimental geometry and the suite of diagnostics used. Constraints on the plasma conditions are derived in Sec. III, where we outline the data reduction and analysis of each diagnostic. In Sec. IV A, we demonstrate that the Sc and Ge spectra obtained early during the expansion show good agreement with steady-state calculations constrained by the measured ion density, while spectra obtained once the plasma has expanded to $n_i \approx 10^{19}$ cm^{-3} are not reproduced by steady-state calculations. In Sec. IV B, we demonstrate that ionization time scales exceed the hydrodynamic timescale, indicating that the Sc ionization has departed from its steady state distribution. After this time, the Sc spectra must be represented by time-dependent calculations.

II. EXPERIMENTAL CONFIGURATION

Targets consisted of a 250-μm-diam Ge:Sc sample centrally buried in a 1000-μm-radius, 10-μm-thick Be tamp (see Fig. 1). The buried layer
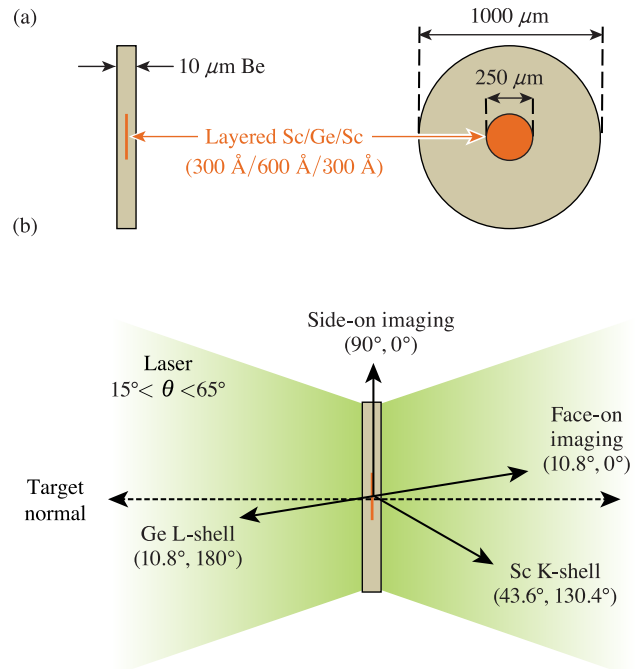

FIG. 1. (a) Cross-sectional views of the target, side-on (left) and face-on (right). The Ge:Sc layer is centrally buried within a 10-μm-thick Be tamp and consists of 0.03 μm Sc, 0.06 μm Ge, and 0.03 μm Sc. (b) Experimental geometry showing representative diagnostic views. Angles (θ, ϕ) denote the polar angle θ from the target normal and the azimuthal angle ϕ in the target plane relative to the side-on imaging view. Lasers irradiate both sides of the target with angles of incidence between 15° and 65°.

consisted of sequentially deposited layers of 0.03 μm Sc, 0.06 μm Ge, and 0.03 μm Sc. The buried layer was kept thin to mitigate axial gradients and help maintain uniform conditions throughout the Ge:Sc sample. To determine the background contribution of the Be tamp and its impurities to the data, targets fabricated without a buried layer were also shot.

The OMEGA-60 laser facility[16] was used to deliver a total of 7.5 kJ of laser energy to both sides of the targets over 3.5 ns using a constant-irradiance drive. Beams were propagated through focus to achieve an approximately 600-μm-diam spot size on the target, providing a drive irradiance of 10^{14} W/cm^2 on each face of the target.

The lasers ablate, burn through, and cause the entire target package to expand primarily along the target normal and heat to keV temperatures. A uniform and slowly decreasing temperature is established within the sample once deposition of laser energy and conduction from the surrounding hot Be reservoir are balanced by mechanical losses from expansion and radiative losses from emission.[10,11] Two-dimensional simulations of similar experiments indicate a high degree of radial and axial uniformity within the sample after the laser burns through the buried layer.[17]

An array of 16 pinholes was coupled to a four-strip x-ray framing camera[18] with a 50-ps integration window to capture time-gated x-ray images of the plasma emission. Two such cameras were deployed looking nearly parallel and perpendicular to the target normal, yielding

face-on and side-on views, respectively, of the expansion, as shown in Fig. 1. These orthogonal views of the x-ray emission of the Ge and Sc are used to determine the average ion density and its evolution during expansion.

Sc K-shell and Ge L-shell spectra are obtained simultaneously with the x-ray images. The spectra were collected by separate multipurpose spectrometers (MSPECs),[19–21] time-gated by x-ray framing cameras with a 200-ps integration window, and recorded on Kodak T-Max 400 film. For convenience, we will refer to the two spectrometers according to the species they were configured to observe, i.e., the Sc spectrometer and the Ge spectrometer. All imaging and spectral measurements were obtained during the laser drive.

III. DATA ANALYSIS
A. x-ray Images

An example of the orthogonal x-ray image sequence is shown in Fig. 2. After subtracting emission from the images due to the Be tamp, the height of the expansion visible in the side-on images is inferred as the full-width at half-maximum (FWHM) of a Gaussian profile. An azimuthally averaged diameter is inferred from the face-on images as the FWHM of a fourth-order super-Gaussian. The Ge and Sc are assumed to homogeneously occupy a cylindrical volume given by the measured height and diameter. The spatially averaged total ion density $n_i = n_{Sc} + n_{Ge}$ is calculated from this volume and the characterized initial mass of the buried layer assuming conservation of particles. Due to the high signal-to-noise ratio in the images, the statistical uncertainty in n_i from fitting the emission volume produces a fractional random uncertainty of $\leq 2.5\%$. Metrology of the initial buried-layer mass gives a fractional systematic uncertainty in n_i of 11%. Uncertainties in the absolute experimental timing are taken as the integration time of the measurement, of order 50 ps. Uncertainties in the time delay between measurements is constrained by the framing camera
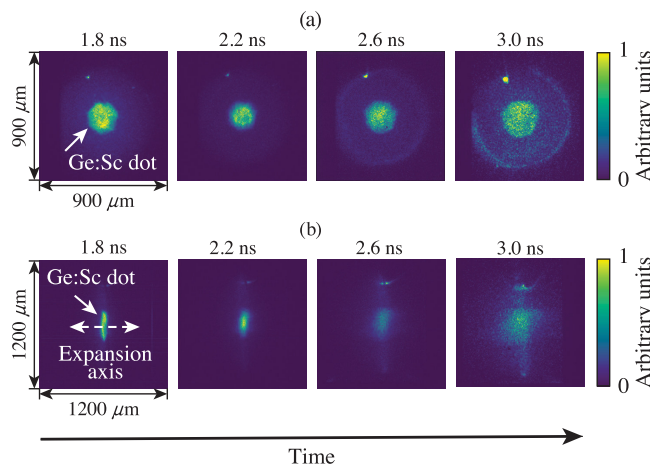
electronics and assumed negligible compared to the absolute timing and integration time.

Extracting ion density from self-emission images using this method has been previously validated against spectroscopic line ratios of Fe:V buried-layer targets.[22,23] In that work, radiative-transfer calculations were used to predict the enhancement of the He-like resonance line ($^1P_1 - {}^1S_0$) over the intercombination line ($^3P_1 - {}^1S_0$) as a function of target viewing angle and aspect ratio of the expanding buried layer. The relative enhancement between spectra obtained from face-on and side-on views of the layer required an ion density consistent with that measured by self-emission images.

B. Sc K-shell spectra

The steady-state mean ionization state $\bar{Z}$ of Sc and Ge at relevant conditions is shown in Fig. 3. Above 1 keV, the Sc $\bar{Z}$ is relatively insensitive to density, while the Ge $\bar{Z}$ retains sensitivity to both density and temperature. Though the Sc $\bar{Z}$ changes little with temperature, the Sc K-shell emission spectrum changes dramatically (Fig. 4), most notably in the intensity of the Ly$_\alpha$ due to an increasing population of the H-like state. Combined with a relative insensitivity to density, the Sc K-shell spectrum is a compelling temperature diagnostic in this regime.

Sc K-shell spectra are processed by accounting for the spectral sensitivity of the spectrometer and framing camera.[21,24,25] Raw and processed data are shown in Fig. 5. Notable lines in the Sc spectra include the H-like series $np - 1s$, the He-like series $1s\,np - 1s^2$, and the Li-like satellites $1s2p\,n\ell - 1s^2n\ell$ on the low-energy side of the He$_\alpha$ complex $1s2p - 1s^2$. We infer the ionization temperature T_Z of the Sc by fitting optically thin regions of the observed Sc K-shell spectra with spectra calculated by SCRAM, assuming steady-state populations. The Li-like satellites and intercombination line of the He$_\alpha$ complex, and the Ly$_\beta$ complexes were estimated by SCRAM to be optically thin. The Sc Ly$_\alpha$ line has an optical depth of 0.9 along the spectrometer line of sight during the earliest measurement, but quickly becomes optically

FIG. 2. (a) Face-on and (b) side-on images of 2–5 keV emission obtained throughout the expansion phase after the laser burned through the Ge:Sc layer of shot S90543. Spatial scales are noted in the first image of each row, and times are listed above each image. The bright Ge:Sc layer is visible inside the diffuse emission of the surrounding Be tamper. The Ge:Sc layer expands horizontally in the side-on images.
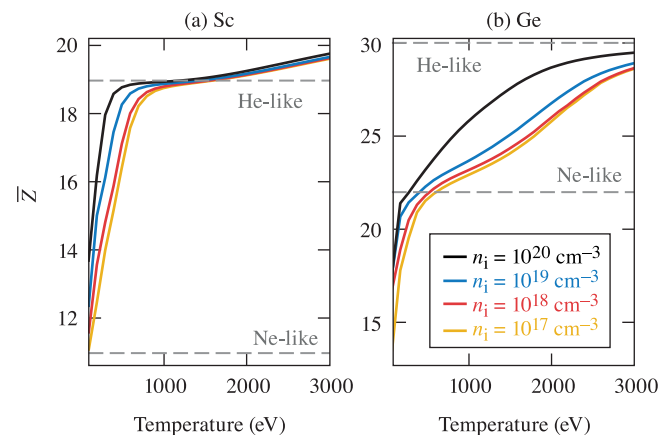

FIG. 3. Mean ionization state $\bar{Z}$ of equilibrium (a) Sc and (b) Ge plotted vs temperature for various densities. For $T_e > 1000$ eV, the $\bar{Z}$ of Sc varies little with density and can be used as a temperature diagnostic with only an estimate of n_i. Interpretation of the $\bar{Z}$ of Ge requires knowledge of n_i to within a factor of 2 for $n_i > 10^{18} \text{cm}^{-3}$.
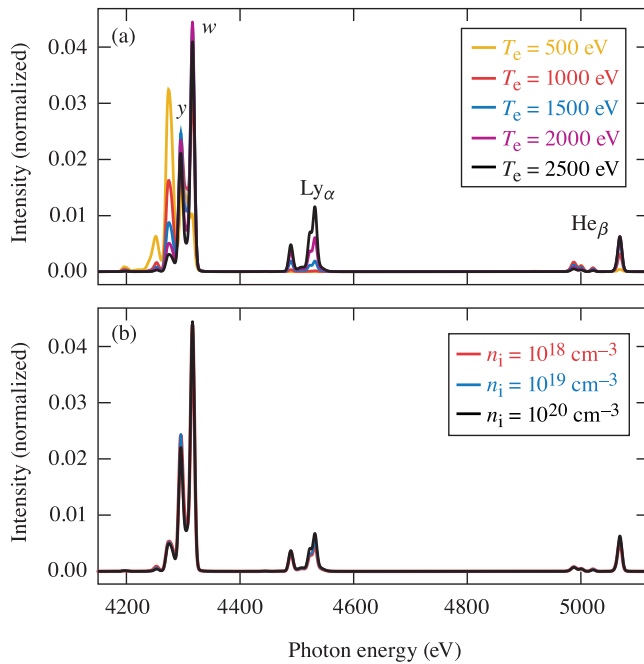
FIG. 4. Portion of steady-state Sc K-shell spectrum calculated by SCRAM (a) for various temperatures at $n_i = 5 \times 10^{19}$ cm^{-3} and (b) for various ion densities at $T_e = 2000$ eV. Labels denote the Ly$_\alpha$ and He$_\beta$ complexes, and the resonance ($^1P_1 - ^1S_0$, w) and intercombination ($^3P_1 - ^1S_0$, y) lines of the He$_\alpha$ complex. The represented conditions bracket those achieved in the experiments. The steady-state Sc spectrum changes almost exclusively with temperature, motivating its use as a temperature diagnostic insensitive to density.
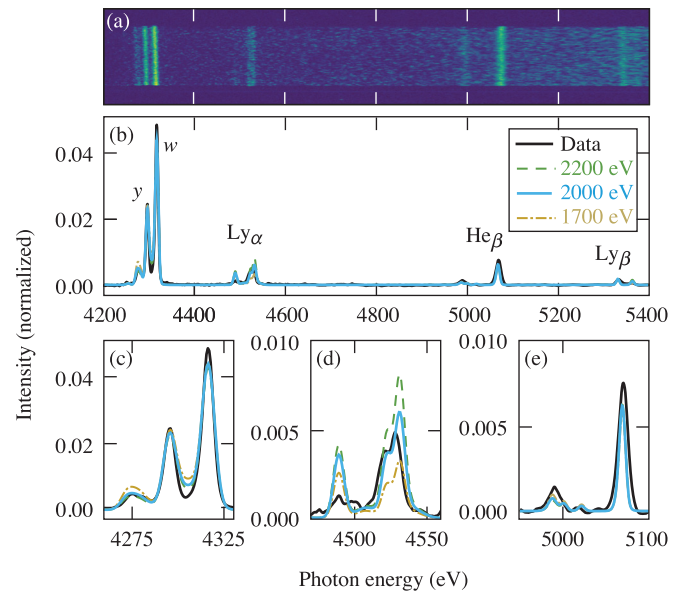

FIG. 5. (a) Raw data and (b) processed spectrum (black) of the Sc K-shell emission at 2.6 ns plotted on the same photon energy axis. Magnified views of various features are shown in (c)–(e). See the caption of Fig. 4 for label definitions. Synthetic spectra are shown at the best fit temperature of 2000 eV (blue) and at the uncertainty bounds of 1700 eV (dash-dotted yellow line) and 2200 eV (dashed green line), indicating that the temperature of the Sc can be determined to 10% using the K-shell spectral analysis. The intensity of the He-like satellite of Ly$_\alpha$ shown in (d) below $h\nu = 4500$ eV is overpredicted by all temperatures.

thin due to expansion. The resonant line (w) of the He$_\alpha$ complex has an optical depth always exceeding 2. The optically thick resonant line and the entire He$_\beta$ complex, as well as the intervening continuum regions, are ignored in the fits.

In the hybrid level structure of SCRAM, level energies and transition rates calculated in an isolated-atom framework by the fully relativistic flexible atomic code[26] are separated into detailed fine structure levels and averaged non-relativistic configurations and superconfigurations.[27] The collisional-radiative rate matrices are then constructed with the level and rate data and solved to determine populations needed to generate spectra. SCRAM generally exhibits good agreement with more detailed codes,[27] though emission features from transitions between averaged levels are less accurate.[28] The neglect of dense plasma effects implicit in using isolated-atom data is justified at the low electron densities of the experiment.[29]

In the following analysis, we find that temperature gradients are not necessary to describe the Sc spectra. A set of single-temperature steady-state spectra were generated from SCRAM and treated as a set of basis vectors to reproduce the observed spectra. Assuming the plasma is optically thin and consists of a distribution of temperatures, the observed spectrum S_x is modeled as a linear sum of the generated spectra $S(T_j, \bar{n}_i)$, each with an unknown abundance (or discretized differential emission measure) a_j,

$$S_x = \sum_j a_j S(T_j, \bar{n}_i), \tag{1}$$

where $\bar{n}_i$ is the average density during the 200-ps integration of the corresponding framing camera. The Sc K-shell spectra are negligibly sensitive to density changes of a factor of 10 (see Fig. 4), such that either small errors or gradients in the density measurement affect the inferred temperature by at most 100 eV (and likely much less). To conserve the number of Ge and Sc atoms in the system, $\sum_j a_j = 1$. The spectral fit is then found by determining the relative abundance a_j of each temperature component T_j.

The inferred abundance distributions that best fit each spectrum assign all of the abundance into a single temperature or two neighboring temperatures. Such unimodal and narrow abundance distributions indicate that each spectrum is well-described by a single-temperature plasma. Figure 5 reveals the ability of a single-temperature spectrum to reproduce the data. For the remainder of the manuscript, the plasma will be treated as single-temperature. χ^2 uncertainty analysis assuming a uniform plasma suggests a 10% uncertainty in the inferred temperature. Synthetic spectra at 1700 and 2200 eV ($\approx \pm 10\%$ of the best-fit temperature) are overlaid in Fig. 5 to demonstrate the sensitivity of this diagnostic to temperature. This analysis is repeated for Sc spectra obtained at multiple times throughout the experiment to determine $T_Z^{Sc}(t)$.

C. Ge L-shell spectra

Ge L-shell spectra were collected and processed in the same manner as the Sc spectra. The processed spectra are shown as black traces in Fig. 6, and identified lines are listed in Table I. A few lines in the Ge
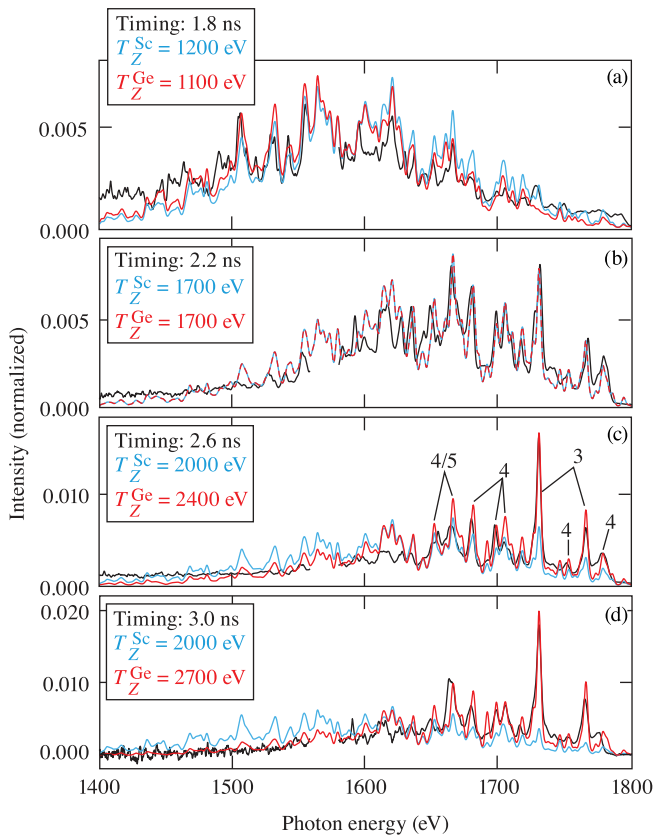
FIG. 6. Observed Ge L-shell spectra (black) at experimental times of (a) 1.8, (b) 2.2, (c) 2.6, and (d) 3.0 ns. Steady-state SCRAM calculations at the corresponding measured temperatures (T_Z^{Sc} in blue and T_Z^{Ge} in red) and densities (see Fig. 7). Temperatures of the SCRAM spectra are included in the legend. All spectra are normalized to the integrated signal in the energy range displayed. Numerical labels indicate the isoelectronic sequence producing prominent features (3 = Li-like, 4 = Be-like, and 5 = B-like). In panels (c) and (d), steady-state calculations at T_Z^{Sc} fail to reproduce the observed Ge spectra after $t = 2.4$ ns.

TABLE I. Transition energies of observed lines from B-, Be-, and Li-like Ge ions as reported by SCRAM. Strong lines visible in the late time Ge L-shell spectra predominantly are due to $3d \rightarrow 2p$ transitions.

Isoelectronic sequence	Upper configuration	Lower configuration	Transition energy (eV)
Li	$3s^1$	$2p^1$	1691.7
Li	$3d^1$	$2p^1$	1730.6
Li	$3d^1$	$2p^1$	1766.0
Be	$2s^1 3d^1$	$2s^1 2p^1$	1666.5
Be	$2p^1 3d^1$	$2p^2$	1669.5
Be	$2p^1 3d^1$	$2p^2$	1679.4
Be	$2p^1 3d^1$	$2p^2$	1681.6
Be	$2s^1 3d^1$	$2s^1 2p^1$	1698.6
Be	$2p^1 3d^1$	$2p^2$	1705.1
B	$2p^2 3d^1$	$2p^3$	1614.7
B	$2p^2 3d^1$	$2p^3$	1616.0
B	$2s^1 2p^1 3d^1$	$2s^1 2p^2$	1635.9
B	$2p^2 3d^1$	$2p^3$	1654.4

predicted envelope agrees with the observed spectra, and line positions are accurately reproduced, most notably the distinct Be- and Li-like lines above $h\nu = 1700$ eV that emerge at 2.2 ns. The kinetics model assigns consistent ionization temperatures to the Ge and Sc during the early expansion phase of the plasma. It is likely that both Sc and Ge have equilibrated to the local plasma conditions, and $T_Z^{Sc} = T_Z^{Ge} = T_e$.

After 2.2 ns, the Ge spectra calculated at T_Z^{Sc} deviate substantially from the observed spectra. Once T_Z^{Sc} and the observed Ge ionization plateau, the SCRAM-predicted Ge ionization distribution recombines in response to the decreasing density of the expanding plasma. Consequently, the strong $3d^1 \rightarrow 2p^1$ Li-like lines at 1730.6 and 1766.0 eV in the synthetic spectra decrease in intensity as the Li-like population decreases, and the envelope of the emission shifts to lower photon energies as less-ionized charge states are populated. In the observed spectra, however, the Li-like lines persist, and the emission envelope does not shift.

The late-time Ge and Sc spectra cannot be modeled with steady-state calculations at a single temperature. In the preceding analysis, we have generated synthetic Ge L-shell spectra at $T_e = T_Z^{Sc}$, and we find disagreement with the observed Ge spectra. We can instead identify temperatures T_Z^{Ge} that describe the Ge spectra (see Fig. 6). Determination of T_Z^{Ge} from the Ge spectra is negligibly influenced by the few optically thick lines because the majority of the spectrum remains optically thin. Uncertainty in T_Z^{Ge} is estimated to be 200 eV. Even accounting for uncertainties, $T_Z^{Ge} > T_Z^{Sc}$ at late times. We note that Sc spectra generated at T_Z^{Ge} substantially overpredict the observed intensity of the Ly$_\alpha$ feature.

IV. BENCHMARKING THE ATOMIC KINETICS MODEL

A. Evolution of conditions

Combining the ion density and ionization temperature analyses, we can reconstruct the evolution of the buried layer through $T_Z - n_i$ space (Fig. 7). Acquisition of (T_Z, n_i) begins at 1.5 ns, after the laser has ablated through the Be tamper and into the buried layer. Arrival of the ablation front at the Ge:Sc layer is signaled both by the bright

spectrum are optically thick. During the earliest measurement, the most optically thick line is a $2p^2 3d - 2p^3$ line of N-like Ge, with a transition energy of 1563.4 eV and an optical depth of 1.7. The subsequent ionization rapidly populates the Li-like state, making a strong $3d - 2p$ Li-like line at 1730.6 eV the most optically thick line, with an optical depth of 3.4 that decreases in time due to expansion. Additionally, a line emission feature at 1570 eV has been removed from the Ge spectra, identified as He$_\alpha$ emission from Ar ($h\nu = 3140$ eV) in the Be tamper that is reflected from the spectrometer crystal in the second order.

We now consider the consistency of the atomic model by calculating steady-state Ge spectra, given the n_i measured from the x-ray images and assuming $T_e = T_Z^{Sc}$. The steady-state calculations are compared to the processed spectra in Fig. 6. Note that complexity of the structure and kinetics calculations for the L-shell spectra is considerably more challenging than for K-shell spectra, and reproduction of line positions and intensities of the L-shell spectra will not be as high of a quality as for the K-shell. At the earlier times (1.8–2.2 ns), the
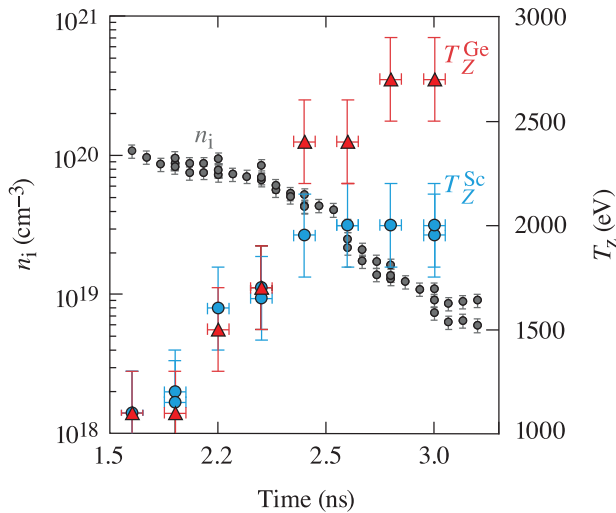
FIG. 7. Ion density (gray circles) inferred from the emitting volume of the expanding targets, and ionization temperatures of Ge (red triangles) and Sc (blue circles) inferred from their respective spectra. Sc and Ge spectral measurements coincide with the temperature data. Measurements from multiple shots are shown.

emission from the Ge:Sc layer visible in the x-ray images and by the increasing ionization evident in the spectra. Direct illumination by the laser causes the buried layer to rapidly heat and expand, as is evident in the n_i and T_Z measurements plotted vs time in Fig. 7. An accelerated decrease in density at 2.5 ns is caused by radial expansion as the pressure equilibrates between the expanding Ge:Sc region and the surrounding Be.[17] This expansion follows a radially inward-propagating density perturbation launched by an increased pressure on the sides of the Ge:Sc layer once the laser burns through the Be tamp but has yet to fully burn through the Ge:Sc. This density perturbation leads to a slight enhancement in x-ray emission, visible as the faint ring of emission inside the Ge:Sc layer at 2.2 ns. Because emissivity scales with n_e^2, the density perturbation is estimated from the ratio between the signal in the ring to the signal interior to the ring to be less than 5%. The radial expansion is visible in the face-on images of Fig. 2.

Prior to 2.4 ns, $T_Z^{Sc} = T_Z^{Ge}$. From the definition of T_Z, we deduce that both Sc and Ge have equilibrated to the local plasma conditions, and $T_Z^{Sc} = T_Z^{Ge} = T_e$. However, at 2.4 ns T_Z^{Sc} plateaus at 2000 eV, while T_Z^{Ge} continues to increase to 2700 eV at 2.8 ns. We attribute this to the onset of a time-dependent, nonequilibrium ionization state in the Sc (see Sec. IV B). We have investigated the effects of the assumptions made in this analysis to confirm that the discrepancy in T_Z is not artificially introduced by the assumptions. We discuss these below.

The absolute density n_i does not affect our conclusions. We have inferred density from the volume of the emitting plasma. Images clearly indicate that the plasma is expanding, so the density must be decreasing throughout the measurements. Steady-state SCRAM calculations predict a lower ionization with decreasing density in the range of 10^{17}–10^{22} ions/cm^3. As such, a different $n_i(t)$ (with the requirement $\frac{dn_i}{dt} < 0$) would still yield recombination in the synthetic spectra. On the contrary, the observed spectra do not change appreciably after 2.2 ns, indicating that the true ionization of Ge does not change in response to the decreasing density. We conclude that an error in the absolute density would not cause the observed inconsistency.

Additionally, the observed inconsistency is not caused by axial gradients. Targets in which the Ge and Sc layer order was inverted also exhibited $T_Z^{Ge} > T_Z^{Sc}$ during the late-phase expansion.

B. Time-dependent Ionization Kinetics

We now consider the possibility of a time-dependent ionization of either Sc or Ge and its impact on the inferred temperatures. The ionization of a species will depart from the steady-state value when the ionization equilibration time τ exceeds the faster of the hydrodynamic timescale τ_{hydro} and the thermal timescale τ_{th},

$$\tau_{hydro} = \left(\frac{1}{n_i}\frac{dn_i}{dt}\right)^{-1}, \tag{2}$$

$$\tau_{th} = \left(\frac{1}{T_e}\frac{dT_e}{dt}\right)^{-1}. \tag{3}$$

We can estimate τ from a simplified system consisting of the ground states of two charge states Z and $Z+1$. Neglecting ionization from excited states (ladder ionization) and three-body recombination, the two charge states are connected by collisional ionization and radiative recombination with respective rate coefficients S and α. Conservation of particles allows definition of the total ion density $n_i = n_Z + n_{Z+1}$ and free electron density $n_e = \bar{Z}n_i$. Solution of the corresponding rate equation

$$\frac{dn_Z}{dt} = n_e[\alpha n_i - (\alpha + S)n_Z], \tag{4}$$

yields the time-dependent population of the recombined state

$$n_Z(t) = \frac{\alpha}{\alpha + S}n_i + Ce^{-n_e(\alpha + S)t}, \tag{5}$$

where C is a constant whose value depends on the populations at $t = 0$. From this, we define the equilibration time as follows:

$$\tau = (n_e(\alpha + S))^{-1}. \tag{6}$$

Note that the scaling of $S \propto (\sqrt{kT}/E_\infty^2) \times e^{-E_\infty/kT}$ indicates that a species with greater ionization potential E_∞ or lower temperature kT will tend toward a larger rate coefficient and a smaller ionization timescale.[30]

Comparison between τ and the smaller of τ_{hydro} and τ_{th} indicates when a system in ionization equilibrium will depart from equilibrium. If plasma conditions change rapidly such that $\tau > \min(\tau_{hydro}, \tau_{th})$, the ionization will take some time (of order τ) to equilibrate to the new state. Thus, the ionization will "lag" the changing conditions. Prior to equilibrating, diagnosis of plasma conditions from the ionization will yield a result intermediate to the old and new conditions. In the extreme case $\tau \to \infty$ at some time t_0, the ionization will not respond to an evolving thermodynamic state, instead appearing to "freeze in" at the state at t_0. For example, if the plasma is then heated, the ionization will indicate too low of a temperature. This is liable to happen in an expanding plasma because the collisional ionization rate $n_e S$ and the radiative recombination rate $n_e \alpha$ decrease with lower density, lengthening the ionization timescale.

We can evaluate τ for the potential limiting ionization and recombination processes in our system. For Sc, we consider if the Sc ionization lags the steady-state value during the heating process, leading to $T_Z^{Sc} < T_e$. Since the observed Sc spectrum is predominantly

07 July 2023 14:53:19

He-like and the steady-state ionization is anticipated to be further ionized, we will evaluate τ between He-like and H-like Sc. For Ge, likewise, we consider if the ionization lags the steady-state value as the plasma expands. A predominant Li-like charge state of Ge and a steady-state ionization that recombines with decreasing density indicates that the recombination of Li-like to Be-like Ge could limit this system. Tabulated values of S and α of the proposed limiting ionization and recombination processes are taken from the OPEN-ADAS database.[31,32] Rate coefficients for Ge were linearly extrapolated from coefficients for Fe through Zn. Collisional-radiative rates within SCRAM were not used in order to make this metric accessible to a broader set of researchers. The only dependence on SCRAM is through determination of the measured T_Z. To calculate n_e in Eq. (6), a constant $\bar{Z} = 24.5$ is assumed, being the average ionization of He-like Sc and Li-like Ge.

In principle, the ionization time scales τ_{Sc} and τ_{Ge}, hydrodynamic timescale τ_{hydro}, and thermodynamic timescale τ_{th} can be calculated directly from the measured T_e and n_i of Fig. 7. However, two issues arise when analytically propagating errors from the measurements. First, systematic uncertainties and temporal correlations artificially inflate the uncertainty of the time derivatives in τ_{hydro} and τ_{th}. Second, use of the tabulated α and S prevent use of analytic approximations of error propagation. Instead, all time scales and their uncertainties were calculated from Monte Carlo error propagation using synthetic T_e and n_i datasets inferred from the experimental measurements.[33] The synthetic datasets were constructed to incorporate temporal correlations between the T_e and n_i measurements of Fig. 7, critical to correctly determine uncertainties of the time derivatives in τ_{hydro} and τ_{th}.

Synthetic density datasets were generated by sampling from the product of two Gaussian distributions $\mathcal{N}(\sigma)$ with unit mean and fractional standard deviations σ corresponding to the random and systematic uncertainties:

$$n_{jk} = n(t_j) \times \mathcal{N}_{jk}(\sigma_{rand}) \times N_k(\sigma_{syst}), \quad (7)$$

where n_{jk} is the sampled ion density at time t_j of the kth synthetic dataset, $n(t_j)$ is the measured ion density at time t_j, and the subscript i has been omitted for clarity. Measurements were generated at $N_j = 8$ times corresponding to the eight T_Z measurements, and for $N_k = 5000$ synthetic datasets to ensure robust sampling of the posterior distributions. The Gaussian distribution N_{jk} accounts for the random uncertainty $\sigma_{rand} = 2\%$ in the individual measurements and is evaluated for each of the $N_j \times N_k$ synthetic measurements. The Gaussian distribution N_k accounts for the systematic uncertainty σ_{syst} of the unknown buried layer mass and is evaluated once for each of the N_k synthetic datasets. A systematic uncertainty of $\sigma_{syst} = 19\%$ is used to incorporate shot-to-shot variability in n_i.

Uncertainties in T_Z are not divisible into random and systematic sources. Using a Pyro-based sampler for Bayesian inference,[34,35] the measured T_Z of Sc and Ge are fit with separate sigmoid functions,

$$T_Z(t) = A\left(1 + e^{-(t-B)/C}\right)^{-1}. \quad (8)$$

Synthetic temperatures are sampled from the resulting posterior predictive distributions. Distributions of the hydrodynamic, thermal, and ionization timescales are calculated from the T_e and n_i samples. The mean and 90% highest-density intervals (HDI) of each distribution is plotted in Fig. 8.

The ionization of both Ge and Sc begin in steady-state due to the higher density and shorter ionization time scales early during the
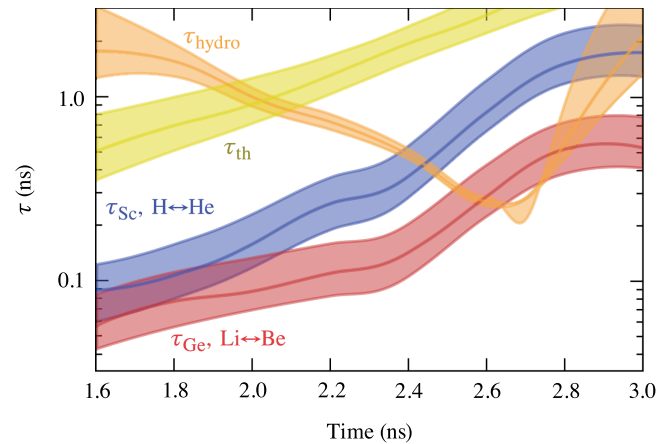

FIG. 8. Ionization equilibration time scales according to Eq. (6) of Sc He- to H-like (blue) and Ge Be- to Li-like (red), hydrodynamic timescale τ_{hydro} (orange), thermal timescale τ_{th} (yellow), and associated 90% HDIs. All time scales are calculated assuming $T_e = T_Z^{Ge}$. τ_{hydro} crosses τ_{Sc} around 2.4 ns, consistent with when $T_Z^{Sc} \neq T_Z^{Ge}$.

expansion. Because measurements were performed once the temperature approached a steady-state, τ_{th} is the longest timescale for all times. Relative to the ionization rate, the temperature is slowly varying. The rate of change of the temperature does not prevent the ionization from reaching a steady state.

As the plasma expands, $\tau_{hydro} < \tau_{Sc}$ for $t > 2.4$ ns, suggesting that the Sc ionization will not equilibrate with the evolving plasma conditions. If the plasma temperature T_e continues to increase while $\tau_{Ge} < \tau_{hydro} < \tau_{Sc}$, a situation will arise where $T_Z^{Sc} < T_Z^{Ge}$, consistent with the inferred T_Z for these times. Ge, having a faster τ by virtue of the smaller ionization potential of its dominant charge state, will exhibit an ionization that follows T_e more closely than that of Sc. Because no independent measurement of T_e was made, we cannot conclusively determine the relationship between T_e and T_Z^{Ge} or the time-dependence of the Ge ionization.

We note that the comparison between τ_{hydro} and τ will indicate when a system initially in ionization equilibrium departs from equilibrium, but it will not indicate how long the system will take to return to equilibrium. To estimate a lower bound for the time to re-establish equilibrium, one can take the value of τ when it falls back below both τ_{hydro} and τ_{th}. For instance, Fig. 8 shows that τ_{hydro} exceeds τ_{Sc} around 3.0 ns; since $\tau_{Sc} \approx 1.5$ ns at this time, we can expect it would take at least 1.5 ns for the Sc ionization to equilibrate with the plasma conditions. Likewise, $\tau_{hydro} > \tau_{Ge} \approx 0.5$ ns at a time of 2.8 ns, and the Ge ionization will take at least 0.5 ns to equilibrate.

As an additional check of the time-dependence, we have performed time-dependent calculations of the atomic state populations and resulting spectra using SCRAM. Time-dependent calculations of the Ge spectra using $T_Z^{Ge}(t)$ closely resemble the corresponding steady-state calculations. According to these calculations, it is unlikely that the Ge ionization is time-dependent. Time-dependent calculations of the Sc spectra were performed for $T_Z^{Sc}(t)$. The calculations indicate a departure from steady state but fail to reproduce the observed Sc spectra. The calculated time-dependent ionization is too slow, and the

Ly_α intensity is lower than observed for all but the latest time. However, Fig. 8 indicates that the Ge ionization may also become time-dependent after 2.6 ns, in which case T_Z^{Ge} becomes an inaccurate metric of T_e. To determine a $T_e - n_i$ trajectory consistent with all measurements, the time-dependent Sc and Ge spectra would need to be generated along an ensemble of plausible $T_e - n_i$ trajectories and analyzed for goodness of fit to the observed Ge and Sc spectra. Such multi-dimensional, multi-objective optimization is beyond the scope of this paper.

V. CONCLUSION

The development of accurate non-LTE atomic spectral models relies on experimental spectra from a characterized source. Few data-sets exist in the literature due to the difficulty of creating and diagnosing non-LTE plasmas. We have presented simultaneous Sc K-shell and Ge L-shell spectra from an expanding buried-layer plasma with measured ion density. The two spectra not only test predictions of the ionization balance of two materials with appreciably different Z, but also provide an *in situ* determination of ionization equilibrium. Sc K-shell and Ge L-shell spectra obtained during the early-phase expansion are successfully reproduced by a steady-state calculation by the atomic kinetics model SCRAM at the measured density and a single temperature. This demonstrates the accuracy of the atomic kinetics model within SCRAM. As the plasma expands, steady-state calculations fail to match both spectra at the same plasma conditions, and we find that $T_Z^{Ge} > T_Z^{Sc}$. Calculations of the thermodynamic and ionization time scales throughout the experiment suggest that T_Z^{Ge} and T_Z^{Sc} diverge once the Sc ionization timescale exceeds the hydrodynamic timescale. The difference in T_Z is, thus, most likely due to a time-dependent ionization state of Sc. The Sc spectra lags behind the rising plasma temperature, resulting in the observed $T_Z^{Ge} > T_Z^{Sc}$. Time-dependent SCRAM calculations were unable to reproduce both spectra.

Rather than signaling the end of a useful measurement, the onset of time-dependence of the Sc ionization poses an important observation for atomic kinetics models to reproduce. The thermodynamic time scales can be experimentally varied to force disequilibrium to occur earlier or later during the experiment to further test the accuracy of kinetics models. Additionally, time-dependent ionization increases the complexity of K-shell temperature diagnostics in expanding plasmas. The possibility of such must be considered carefully when using ionization-based plasma diagnostics at low densities.

The results of this study indicate the value of L-shell emission as a temperature diagnostic, with certain advantages over traditional K-shell diagnostics. The equivalence between T_Z^{Sc} and T_Z^{Ge} while the ionizations are in steady state validates the use of Ge L-shell spectra as a plasma thermometer. The proposed metric of ionization equilibrium indicates that an L-shell species will remain in equilibrium to lower densities than a K-shell species. Finally, L-shell emission spectra can be more sensitive to changes in temperature; L-shell ions exhibit a greater change in $\bar{Z}$ and in the spectrum for a given change in temperature due to the similarity in ionization potential for L-shell ionization states of a given species. When density measurements are available, L-shell spectroscopy should be viewed as an appealing temperature diagnostic.

AUTHOR DECLARATIONS
Conflict of Interest

The authors have no conflicts to disclose.

Author Contributions

David Thomas Bishel: Data curation (equal); Formal analysis (lead); Methodology (supporting); Software (lead); Visualization (lead); Writing – original draft (lead); Writing – review & editing (lead). **Gabriel Perez-Callejo:** Writing – review & editing (supporting). **Philip M. Nilson:** Funding acquisition (equal); Supervision (equal); Writing – original draft (supporting); Writing – review & editing (supporting). **David Alexander Chin:** Formal analysis (supporting); Writing – review & editing (supporting). **James Ryan Rygg:** Supervision (equal); Writing – original draft (supporting); Writing – review & editing (supporting). **Gilbert Collins:** Supervision (equal); Writing – original draft (supporting); Writing – review & editing (supporting). **Edward von Marley:** Conceptualization (lead); Data curation (equal); Formal analysis (supporting); Funding acquisition (supporting); Investigation (lead); Methodology (lead); Project administration (lead); Supervision (equal); Writing – original draft (supporting); Writing – review & editing (supporting). **Marilyn Schneider:** Conceptualization (supporting); Funding acquisition (equal); Resources (lead); Writing – review & editing (supporting). **D. A. Liedahl:** Conceptualization (supporting); Methodology (supporting); Writing – review & editing (supporting). **Robert F. Heeter:** Conceptualization (supporting); Methodology (supporting). **Mark E. Foord:** Conceptualization (supporting); Methodology (supporting). **Gregory Elijah Kemp:** Conceptualization (supporting); Methodology (supporting). **Yechiel Frank:** Methodology (supporting). **James Emig:** Investigation (supporting).

DATA AVAILABILITY

The data that support the findings of this study are available from the corresponding author upon reasonable request.

07 July 2023 14:53:19

REFERENCES

[1] H. K. Chung and R. W. Lee, High Energy Density Phys. **5**, 1–14 (2009).

[2] H. A. Scott and S. B. Hansen, High Energy Density Phys. **6**, 39 (2010).

[3] R. Piron, F. Gilleron, Y. Aglitskiy, H. K. Chung, C. J. Fontes, S. B. Hansen, O. Marchuk, H. A. Scott, E. Stambulchik, and Y. Ralchenko, High Energy Density Phys. **23**, 38 (2017).

[4] S. B. Hansen, H. K. Chung, C. J. Fontes, Y. Ralchenko, H. A. Scott, and E. Stambulchik, High Energy Density Phys. **35**, 100693 (2020).

[5] R. F. Heeter, S. B. Hansen, K. B. Fournier, M. E. Foord, D. H. Froula, A. J. MacKinnon, M. J. May, M. B. Schneider, and B. K. F. Young, Phys. Rev. Lett. **99**, 195001 (2007).

[6] M. J. Herbst, P. G. Burkhalter, J. Grun, R. R. Whitlock, and M. Fink, Rev. Sci. Instrum. **53**, 1418 (1982).

[7] P. G. Burkhalter, M. J. Herbst, D. Duston, J. Gardner, M. Emery, R. R. Whitlock, J. Grun, J. P. Apruzese, and J. Davis, Phys. Fluids **26**, 3650 (1983).

[8] R. L. Kauffman, R. W. Lee, and K. Estabrook, Phys. Rev. A **35**, 4286 (1987).

[9] L. Aschke, S. Depierreux, K. G. Estabrook, K. B. Fournier, J. Fuchs, S. Glenzer, R. W. Lee, W. Rozmus, R. S. Thoe, and P. E. Young, J. Quant. Spectrosc. Radiat. Transfer **65**, 23 (2000).

[10] M. E. Foord, S. H. Glenzer, R. S. Thoe, K. L. Wong, K. B. Fournier, J. R. Albritton, B. G. Wilson, and P. T. Springer, J. Quant. Spectrosc. Radiat. Transfer **65**, 231 (2000).

[11] M. E. Foord, S. H. Glenzer, R. S. Thoe, K. L. Wong, K. B. Fournier, B. G. Wilson, and P. T. Springer, Phys. Rev. Lett. **85**, 992 (2000).

[12] T. D. Shepard, C. A. Back, D. H. Kalantar, R. L. Kauffman, C. J. Keane, D. E. Klem, B. F. Lasinski, B. J. MacGowan, L. V. Powers, L. J. Suter, R. E. Turner, B. H. Failor, and W. W. Hsing, Phys. Rev. E **53**, 5291 (1996).

[13] D. M. Chambers, P. A. Pinto, J. Hawreliak, I. R. Al'Miev, A. Gouveia, P. Sondhauss, E. Wolfrum, J. S. Wark, S. H. Glenzer, R. W. Lee, P. E. Young, O. Renner, R. S. Marjoribanks, and S. Topping, Phys. Rev. E **66**, 026410 (2002).

[14] E. V. Marley, D. A. Liedahl, M. B. Schneider, R. F. Heeter, L. C. Jarrott, C. W. Mauche, G. E. Kemp, M. E. Foord, Y. Frank, K. Widmann, and J. Emig, Rev. Sci. Instrum. **89**, 10F106 (2018).

[15] S. B. Hansen, Ph.D. thesis, University of Nevada, Reno, 2003.

[16] T. R. Boehly, D. L. Brown, R. S. Craxton, R. L. Keck, J. P. Knauer, J. H. Kelly, T. J. Kessler, S. A. Kumpan, S. J. Loucks, S. A. Letzring, F. J. Marshall, R. L. McCrory, S. F. Morse, W. Seka, J. M. Soures, and C. P. Verdon, Opt. Commun. **133**, 495 (1997).

[17] Y. Frank, G. E. Kemp, E. V. Marley, G. P. Callejo, M. E. Foord, M. B. Schneider, Y. Ehrlich, and M. Fraenkel, Phys. Plasmas **27**, 063301 (2020).

[18] J. D. Kilkenny, Laser Part. Beams **9**, 49 (1991).

[19] M. May, R. Heeter, and J. Emig, Rev. Sci. Instrum. **75**, 3740 (2004).

[20] R. F. Heeter, J. A. Emig, K. B. Fournier, S. B. Hansen, M. J. May, and B. K. F. Young, Rev. Sci. Instrum. **75**, 3762 (2004).

[21] R. E. Marrs, G. V. Brown, J. A. Emig, and R. F. Heeter, Rev. Sci. Instrum. **85**, 11D626 (2014).

[22] G. Pérez-Callejo, D. A. Liedahl, M. B. Schneider, S. J. Rose, and J. S. Wark, High Energy Density Phys. **30**, 45 (2019).

[23] G. Pérez-Callejo, L. C. Jarrott, D. A. Liedahl, E. V. Marley, G. E. Kemp, R. F. Heeter, J. A. Emig, M. E. Foord, K. Widmann, J. Jaquez, H. Huang, S. J. Rose, J. S. Wark, and M. B. Schneider, Phys. Plasmas **26**, 063302 (2019).

[24] O. L. Landen, A. Lobban, T. Tutt, P. M. Bell, R. Costa, D. R. Hargrove, and F. Ze, Rev. Sci. Instrum. **72**, 709 (2001).

[25] G. A. Rochau, J. E. Bailey, G. A. Chandler, T. J. Nash, D. S. Nielsen, G. S. Dunham, O. F. Garcia, N. R. Joseph, J. W. Keister, M. J. Madlener, D. V. Morgan, K. J. Moy, and M. Wu, Rev. Sci. Instrum. **77**, 10E323 (2006).

[26] M. F. Gu, Can. J. Phys. **86**, 675 (2008).

[27] S. B. Hansen, J. Bauche, C. Bauche-Arnoult, and M. F. Gu, High Energy Density Phys. **3**, 109 (2007).

[28] S. B. Hansen, J. Colgan, A. Y. Faenov, J. Abdallah, S. A. Pikuz, I. Y. Skobelev, E. Wagenaars, N. Booth, O. Culfa, R. J. Dance, G. J. Tallents, R. G. Evans, R. J. Gray, T. Kaempfer, K. L. Lancaster, P. McKenna, A. K. Rossall, K. S. Schulze, I. Uschmann, A. G. Zhidkov, and N. C. Woolsey, Phys. Plasmas **21**, 031213 (2014).

[29] C. R. Stillman, P. M. Nilson, S. T. Ivancic, I. E. Golovkin, C. Mileham, I. A. Begishev, and D. H. Froula, Phys. Rev. E **95**, 063204 (2017).

[30] H. R. Griem, "Principles of plasma spectroscopy," in *Cambridge Monographs on Plasma Physics*, edited by M. G. Haines, K. I. Hopkraft, I. H. Hutchinson, C. M. Surko, and K. Schindler (Cambridge University Press, Cambridge, UK, 2005).

[31] H. P. Summers, "The ADAS User Manual, version 2.6," http://www.adas.ac.uk (2004).

[32] See http://open.adas.ac.uk/ for radiative recombination rate coefficients (ADF48) and collisional ionization rate coefficients (ADF07).

[33] A. Possolo and H. K. Iyer, Rev. Sci. Instrum. **88**, 011301 (2017).

[34] D. Sivia and J. Skilling, *Data Analysis: A Bayesian Tutorial*, 2nd ed. (Oxford Science Publications, Oxford, United Kingdom, 2012).

[35] E. Bingham, J. P. Chen, M. Jankowiak, F. Obermeyer, N. Pradhan, T. Karaletsos, R. Singh, P. Szerlip, P. Horsfall, and N. D. Goodman, J. Mach. Learn. Res. **20**, 1–6 (2019).